Laser & Photonics Reviews

LASER & PHOTONICS REVIEWS

www.lpr-journal.org

RESEARCH ARTICLE

Sub-Diffraction Optical Confinement for Enhanced Second-Harmonic Generation in Suspended Thin-Film Lithium Niobate Nano-Cavity

Zengya Li[1,2,3] | Zhuoran Hu[1,2] | Weihao Wu[1,2] | Guangfeng Wang[1,2] | Hao Li[1,2] | Shijie Liu[1,2] | Bo Wang[1,2] | Yuanlin Zheng[1,2,4] | Xianfeng Chen[1,2,4,5]

[1]State Key Laboratory of Micro-Nano Engineering Science, School of Physics and Astronomy, Shanghai Jiao Tong University, Shanghai, China | [2]State Key Laboratory of Photonics and Communications, Shanghai Jiao Tong University, Shanghai, China | [3]Department of Physics, Chalmers University of Technology, Göteborg, Sweden | [4]Shanghai Research Center for Quantum Sciences, Shanghai, China | [5]Collaborative Innovation Center of Light Manipulations and Applications, Shandong Normal University, Jinan, China

Correspondence: Yuanlin Zheng (ylzheng@sjtu.edu.cn) | Xianfeng Chen (xfchen@sjtu.edu.cn)

Received: 3 December 2025 | **Revised:** 9 April 2026 | **Accepted:** 20 April 2026

Keywords: deep subwavelength | nano cavity | second-harmonic generation | sub-diffraction enhancement | thin-film lithium niobate

ABSTRACT

Confining light beyond the diffraction limit is critical in a plethora of important applications, including nano-lasing, sensing, imaging, and particularly nonlinear optics, as it is essential for enhancing conversion efficiency. Plasmonic resonances can provide superior field confinement, but inherently suffer from ohmic losses and thermal damage. Implementing deep-subwavelength optical confinement in all-dielectric materials for enhanced light-matter interactions devoid of these drawbacks is appealing yet challenging. Here, we demonstrate significant enhancement of second-harmonic generation (SHG) in a bowtie nanostructure embedded within a suspended thin-film lithium niobate (TFLN) circular Bragg grating (CBG) cavity. The ultrasmall mode volume reaches less than $0.001(\lambda/n)^3$. The CBG nanocavity exhibits a high normalized conversion efficiency of 0.85×10^{-2} cm^2GW^{-1} under the pump intensity of 1 $MWcm^{-2}$. An SHG enhancement factor of approximately 3,720 compared to bare TFLN is realized. This approach paves the way for nonlinear nanodevices for robust sub-diffraction light–matter interaction in an ultra-compact and lossless dielectric platform.

1 | Introduction

Light confinement at the deep-subwavelength, and even atomic scale, has long represented a fundamental challenge and a focal point of ongoing research in nanophotonics. The ability to spatially localize photons with extreme precision has opened new avenues for the realization of nanoscale lasers [1, 2], single-molecule sensing [3], superresolution imaging [4], as well as high-efficiency nonlinear and quantum optical devices [5–9]. Achieving such confinement typically requires carefully engineered nanostructures by leveraging optical resonances that can overcome the optical diffraction limit while minimizing optical losses.

Plasmonic resonances, which achieve strong field confinement by coupling light with the collective oscillation of free electrons in metals, can break the optical diffraction limit and enhance light-matter interactions at deep-subwavelength scales [5, 10–12]. Although plasmonic structures possess small mode volumes [11–19], their high ohmic loss, low damage thresholds, and

Zengya Li and Zhuoran Hu contributed equally to this work.

lack of bulk second-order nonlinearity often result in limited nonlinear conversion efficiency. On the other hand, dielectrics with ultralow loss are ideal for nonlinear wave mixings in nanophotonics, and the enhancement can be achieved using various optical resonance schemes. Efforts aimed at replacing metals with all-dielectric materials has led to encouraging progress for enhanced frequency conversion in nanophotonics. Especially, the rise of all-dielectric metasurfaces in recent years–taking advantage of photonic crystals (PhC) [20–24], bound states in the continuum (BICs) [25–27], Mie resonances [28–30], guided-mode resonances (GMR) [31] and anapole resonances [32–35]–has significantly improved the second-order nonlinear conversion efficiency. Nevertheless, these approaches remain constrained by the diffraction limit.

This constraint originates from the widely held belief that dielectric materials in the optical band cannot achieve sub-diffraction confinement [36, 37]. The fundamental obstacle also lies in the fact that dielectric materials typically have dielectric constants below ten at the optical band. However, recent research has shown that an all-dielectric bowtie structure integrated within a PhC cavity can break the diffraction limit and confine light into the atomic scale [2, 38–42]. This optical localization arises from self-similar electromagnetic boundary conditions, which have been explored in passive optical devices. More recently, it has been theoretically attributed to a highly confined electric-field singularity at the apices of the dielectric bowtie nanoantenna, resulting from a divergence in the photonic momentum. This mechanism has already been experimentally employed in the realization of nano-lasers that break the optical diffraction limit [2]. However, nonlinear and quantum optical effects under sub-diffraction confinement remain unexplored and have not yet been demonstrated experimentally. Such ultra-strong light–matter interactions at room temperature open new possibilities for nano-scale nonlinear and quantum optical applications.

As a classical nonlinear material, lithium niobate (LN) has been widely used in nonlinear optics. Thin-film lithium niobate (TFLN), distinguished by its large second-order nonlinear susceptibility, strong electro-optic response, and ultra-low optical loss, has become a material of considerable interest for integrated nonlinear and quantum photonic applications in recent years [43–45]. Nonetheless, in comparison to 2D materials and high-index semiconductors [25, 26, 34], the moderate refractive index of LN ($n_o = 2.21, n_e = 2.14$@1550 nm) imposes limitations on the achievable quality (Q) factors of nanoscale optical resonators. To circumvent this limitation, circular Bragg grating (CBG), which is intrinsically compatible with low-index platforms, have been implemented in TFLN-based nanophotonic structures [46]. Beyond enabling high-Q confinement, CBGs also facilitate efficient photon extraction and enhanced optical field localization, offering significant advantages for nonlinear frequency conversion and quantum light–matter interaction processes [47, 48].

Here, we demonstrate significant SHG enhancement in suspended deep-subwavelength dielectric nonlinear cavity. The design involves a bowtie nanoantenna embedded within a TFLN suspended CBG cavity, enabling highly efficient SHG at the deep-subwavelength scale. By removing the underlying silica substrate, we effectively enhance the refractive index contrast, which leads to a significant improvement in the nanocavity–s optical Q factor. Through a combination of theoretical analysis and experimental validation, we demonstrate the reliability of our design, achieving a maximum experimental Q factor of 370 at the near-infrared (NIR) regime. After integrating the bowtie nanoantenna, the Q factor decreases slightly. The bowtie-embedded CBG cavity yields a 3.8×10^3-fold SHG enhancement factor compared to unstructured TFLN, with a high normalized conversion efficiency of 0.85×10^{-2} $\mathrm{cm^2GW^{-1}}$ under a pump intensity of 1 $\mathrm{MWcm^{-2}}$. The theoretical mode volume reaches as small as $6.96 \times 10^{-4}\,(\lambda/n)^3$, showing extreme light confinement. This strategy opens new opportunities for the development of integrated nonlinear or quantum photonic nanodevices and is expected to advance nanophotonics based on all-dielectric materials, such as nonlinear crystals, semiconductors, and 2D materials.

2 | Working Principle of Sub-Diffraction Optical Confinement in Suspended Dielectric Cavities

In conventional dielectric optical cavities, SHG enhancement is typically constrained by the optical diffraction limit. However, introducing singular structures within the cavity can localize the optical field to deep-subwavelength scales. This extreme confinement originates from the field singularities at specific points, which correspond to the infinite solutions of the second kind Bessel function in cylindrical coordinates, governing the modal distribution in such nanocavities, see also Supporting Information for details of the electric field analysis of suspended dielectric cavities. This sub-diffraction light localization drastically reduces the mode volume, thereby strengthening light–matter interactions and enhancing second-harmonic generation.

Thin-film lithium niobate suffers from increased radiation loss due to a moderate refractive index contrast with the underlying substrate, as compared with silicon on insulator. To address this limitation, a suspended CBG structure is introduced, as illustrated in Figure 1a. This suspended configuration significantly enhances optical confinement in the out-of-plane direction, thereby improving the Q factor. For the investigation in the NIR range, a second-order Bragg grating is employed to accommodate the fabrication constraints of TFLN and to reduce sensitivity to structural imperfections. The grating period is set to $P = 2\Lambda$ with a duty cycle of D (Λ is the first-order Bragg grating period). Additionally, the central nanopillar is carefully designed with a length of $3n_{\mathrm{eff}}\Lambda/2$ to satisfy the condition for anapole resonance, where n_{eff} is the effective refractive index.

To harness the deep-subwavelength enhancement effect, we integrate a bowtie nanoantenna into the suspended circular Bragg grating structure, enabling further enhancement of field confinement and nonlinear conversion efficiency. The schematic of the suspended CBG nanocavity on TFLN is shown in Figure 1b. The bowtie nanoantenna is composed of a pair of 120° sector-shaped apertures, each with a radius of r, separated by a nanogap of G. Notably, the radius r must be carefully controlled. It can disrupt the circular Bragg resonance if r is too large, leading to a significant reduction in the Q factor. In this work, the designed bowtie nanoantenna features a radius $r = 260$ nm and a minimum gap size $G = 20$ nm.

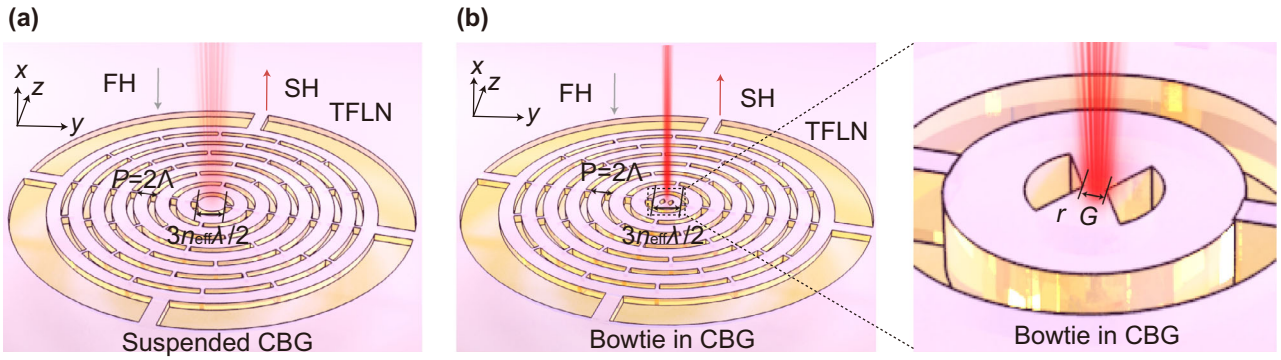

FIGURE 1 | Working principle of deep-subwavelength dielectric nonlinear cavity. (a) Schematic of the suspended CBG on TFLN with anapole resonance. (b) Schematic of the bowtie in CBG on TFLN with deep-subwavelength resonance.

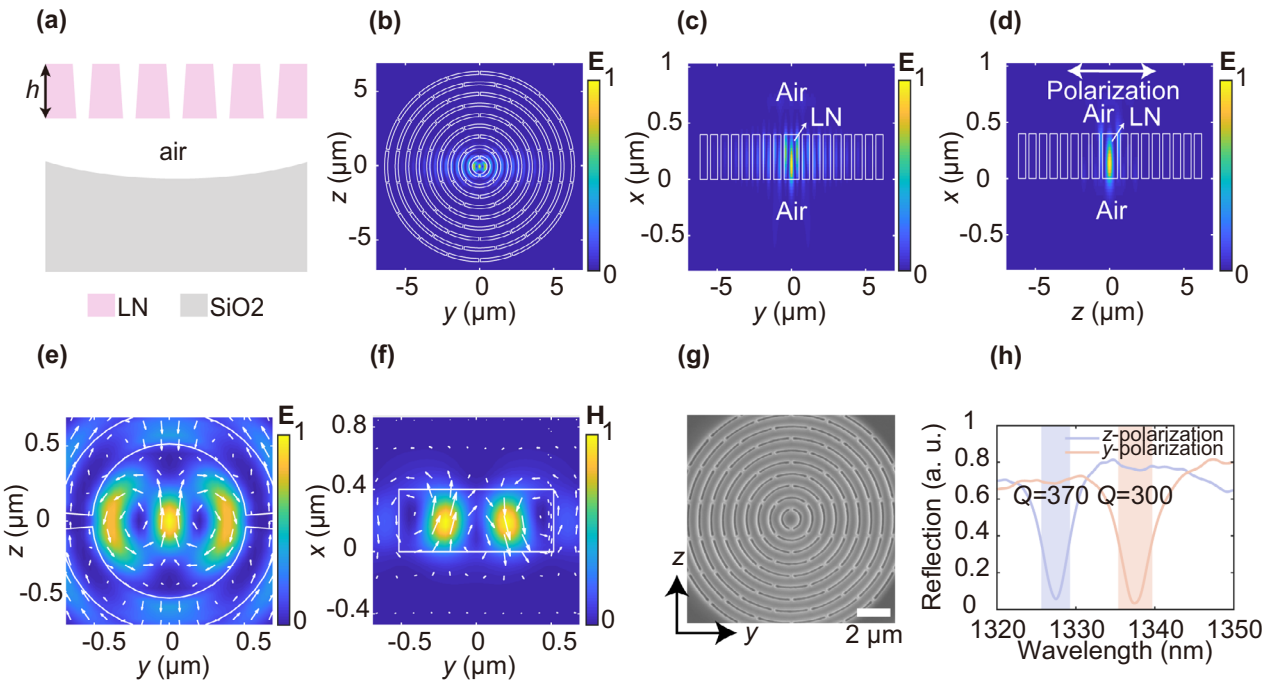

FIGURE 2 | Anapole-mode-enhanced light confinement in suspended CBG cavity. (a) Side view of the suspended CBG cavity. (b–d) *yz*, *xy*, and *xz* cross-sectional views of the electric field at the resonant wavelength of 1327 nm. (e,f) Electric and magnetic field distribution at the anapole resonant wavelength of 1327 nm. (g) SEM images of the fabricated suspended CBG cavity. (h) Experimental reflection spectrum with the period of 740 nm and duty cycle of 0.66 shows a *Q* factor of 370 (300) for *z*-polarized (*y*-polarized) light excitation.

3 | Results and Discussion

3.1 | Anapole-Mode-Enhanced Light Confinement in Suspended CBG Cavity

The side view of the suspended CBG cavity is shown in Figure 2a. The sample is fabricated on a commercially available 400-nm x-cut LN film ($h = 400$ nm) bonded on a 4.7-μm-thick silica buffering layer and a 500-μm-thick silicon substrate (NANOLN, inc.). The undercut structure is fully suspended, i.e., the beneath buffering silica is removed. Selective etching technique is employed to fully suspend the structure without causing collapse or damage. The detailed fabrication process is provided in Methods. The suspended CBG structure is designed to overcome the limited refractive index contrast between LN and silica. This suspended configuration enhances optical confinement in the out-of-plane direction with an improved *Q* factor. By reducing the width of the supporting bars, the *Q* factor can be further increased. The supports are set to be 90 nm wide, to ensure structural strength and weak light scattering, see also Figure S4. Additionally, LN is notoriously difficult for etching with a small sidewall angle (typically 60–80°). As shown in Figure S5, the sidewall angle increases with increasing duty cycle, indicating improved etching sidewall for larger duty cycles. The reflection spectra of the suspended CBG on TFLN are characterized using a supercontinuum laser source in the NIR range. A detailed description of the spectral measurement can be found in the Methods Section and Supporting Information. Gratings with different periods and duty

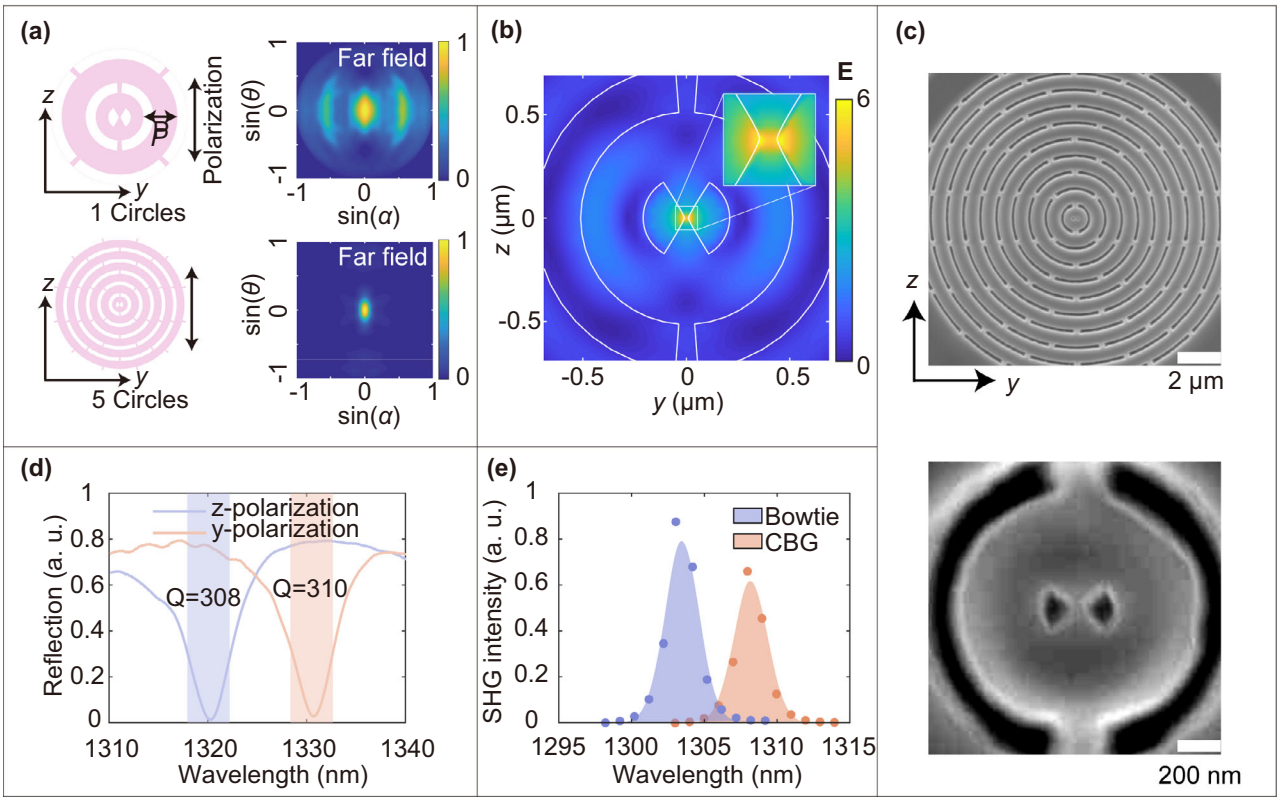

FIGURE 3 | Sub-diffraction light confinement in bowtie-embedded suspended CBG cavity. (a) Simulated far-field radiation patterns of the suspended CBGs with two and six concentric Bragg rings. (b) Electric field distribution of the bowtie embedded nano-cavity with strong light confinement at the nanoantenna center (inset: enlarged electric field). (c) SEM images of the fabricated CBG nanocavity on TFLN with a bowtie nanoantenna positioned at the center. SEM images of the fabricated CBG nanocavity on TFLN with a bowtie nanoantenna positioned at the center. The top panel shows the overall structure (scale bar: 2 μm), while the bottom panel presents a magnified view of the central bowtie (scale bar: 200 nm). (d) Experimental reflection spectrum of the sample with the period of 740 nm and duty cycle of 0.66 shows a *Q* factor of 308 for z-polarized light excitation and 310 for y-polarized light excitation. (e) SHG enhancement in suspended CBG and bowtie-in-suspended CBG Structures.

cycles are used to investigate different resonance conditions, i.e., the spectral positions of the reflection dips (see also the Figures S6 and S7). Importantly, the observed reflection features arise from modifications of the scattering response of the structure under external excitation, rather than from direct far-field radiation of the anapole mode itself.

In the experiment, the suspended CBG exhibits strong electric field confinement and supports anapole resonance. The simulated localized electric field of the fundamental harmonic (FH) wave is mostly confined in the central nanodisk at the resonant wavelength of 1327 nm, as shown in Figure 2b–d. The resonance at the center is identified as a non-radiative anapole mode. As illustrated in Figure 2e,f, the destructive interference between the radiation modes of the electric dipole and toroidal dipole moments at 1327 nm leads to the suppressed far-field radiation, a hallmark of the anapole state. This non-radiative nature results in strong field confinement within the structure, making it highly favorable for enhancing nonlinear optical effects. The suspended CBG is fabricated through a streamlined process involving plasma-enhanced chemical vapor deposition (PECVD), electron beam lithography (EBL), inductively coupled plasma (ICP) etching, and wet etching, with a scanning electron microscope (SEM) image of the sample presented in Figure 2g. A detailed description of the fabrication procedure can be found in the Methods Section and Supporting Information. Furthermore, owing to the suspended configuration, the fabricated circular Bragg cavity exhibits a significantly enhanced *Q* factor, as shown in Figure 2h. Due to the anisotropy of LN, the resonant wavelength exhibits polarization-dependent shifts under excitation by the FH pump light along the *z*- and *y*-polarization directions. The highest measured *Q* factors reach 370 and 300, respectively, representing a significant improvement over our previous work [46], where a *Q* factor of 260 was achieved.

3.2 | Sub-Diffraction Light Confinement in Bowtie-Embedded Suspended CBG Cavity

We integrate a bowtie nanoantenna into the suspended circular Bragg grating structure, enabling further enhancement of field confinement and nonlinear conversion efficiency. The reflection spectra of the bowtie structure embedded in the suspended CBG on TFLN, with grating periods (*P*) ranging from 720 to 820 nm, are characterized. By varying the grating periods and duty cycles, the resonance peak positions can be effectively tuned, enabling the device to satisfy a range of resonance conditions. The measured reflection spectra exhibit a clear redshift of the resonance wavelength with respect to the increasing grating periods, consistent with theoretical predictions, see also Figure S8.

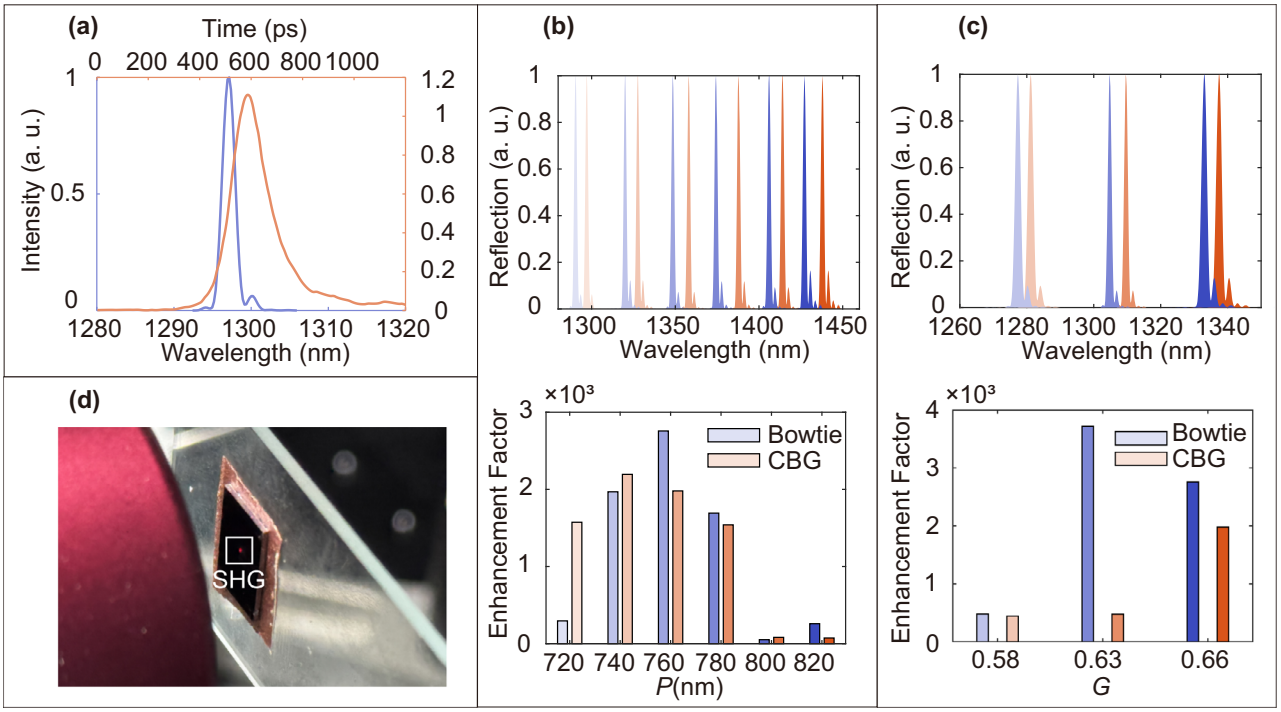

FIGURE 4 | SHG and enhancement in the TFLN nanocavity sample. (a) Spectral and temporal profiles of the pump light. (b) SHG enhancement of suspended TFLN resonator with the periods of 720, 740, 760, 780, 800, and 820 nm. Blue denotes the Bowtie-in-CBG structure, and red denotes the suspended CBG without the bowtie. (c) SHG enhancement of suspended TFLN resonators with duty cycles of 0.58, 0.63, and 0.66, and a fixed grating period of 760 nm. (d) Experimentally observed visible SHG signal from the nanocavity sample.

In addition to compactness, the circular Bragg configuration also demonstrates remarkably superior photon collection efficiency. As illustrated in Figure 3a, when the nanocavity comprises only one concentric rings, the far-field energy distribution is highly divergent. In contrast, the inclusion of five rings results in a far-field energy concentration confined within an angular range of less than ten degrees in the momentum space. This behavior confirms that the suspended CBG structure achieves exceptional compactness, with a minimal footprint down to 10 μm. Additionally, its excellent nonlinear performance and substantially reduced fabrication costs enhance its advantages in multiphoton manipulation, paving the way for compact photon entanglement at room temperature.

As illustrated in Figure 3b, simulation results indicate that the electric field is primarily localized at the nanoantenna's apices, demonstrating a further approximate sixfold enhancement relative to the suspended CBG without the bowtie structure. To prevent a non-convergent solution, the apices of bowtie is designed with a 20 nm-radius arc, and the actual fabricated results closely correspond to this design. As the gap increases, the electric-field enhancement factor gradually decreases (see Figures S10 and S11). In contrast, no pronounced magnetic-field enhancement is observed. The field enhancement originates from electric-field singularities at the sharp tips and within the nanogap region, leading to pronounced electric-field localization. Magnetic-field confinement, however, generally requires circulating displacement currents forming closed loops, which are not supported by the bowtie geometry. Therefore, the enhancement in the bowtie structure is dominated by electric-field localization.

Additionally, we calculated the mode volume by performing the following volume integral on the computed electromagnetic field obtained via the finite-difference time-domain method, $V_m = \frac{\int \varepsilon \mathbf{E}^2 \, dV}{\max(\varepsilon \mathbf{E}^2)}$, where ε is the local permittivity distribution, and $\mathbf{E}$ is the electric field amplitude. The integration is performed over the localized mode region near the bowtie tip. The calculated mode volume is $6.96 \times 10^{-4} \, (\lambda/n)^3$. This shows the structure significantly enhances electromagnetic field localization beyond the diffraction limit. Such an ultra-small mode volume significantly enhances light-matter interaction, which can be exploited to boost the efficiency of SHG, and pave the way for the exploration of nonlinear optical phenomena in the sub-diffraction regime.

The bowtie-in-CBG structure is fabricated by introducing a gradient in the segment spacing. SEM images of the fabricated structure are shown in Figure 3c, while a detailed view of the gradient spacing is provided in Figure S12. As shown in the lower panel of Figure 3c, the scale bar corresponds to 200 nm, and the minimum gap is close to 20 nm, representing the best fabrication result achieved on TFLN to date and enabling subwavelength light confinement. However, due to the sidewall taper introduced during etching, the gap may locally shrink to nearly 0 nm at the edge of the structure.

The fabricated bowtie structure embedded in the suspended CBG exhibits high Q factors of 308 and 310 under z- and y-polarized light excitation, respectively, as shown in Figure 3d. Compared to the suspended CBG without the bowtie nanoantenna, the Q factors are only slightly reduced. It is expected that further reduction of the bowtie size will lead to an increase in the Q

factors. These results indicate that the incorporation of the bowtie structure does not significantly compromise the device–s Q factor.

Compared to the suspended CBG without the bowtie structure, the bowtie-in-CBG exhibits a higher SHG enhancement, as shown in Figure 3e. In fact, the SHG enhancement factor is even higher at the bowtie tips, which requires detection using scanning near-field optical microscopy. From the Supporting Information of nonlinear coupling wave equation and SHG enhancement, it can be deduced that the conversion efficiency satisfies $\frac{P_2}{P_1^2} \propto Q_2 Q_1^2 |\beta|^2$. The nonlinear coupling coefficient β characterizes the efficiency of SH and FH waves within the composite cavity. Specifically, β_1 quantifies the coupling from the FH mode to the SH mode, taking into account contributions from both the hotspot and non-hotspot regions, while β_2 emphasizes the contribution of the SH mode to FH mode.

Based on Equation (S24), we further derive the relationship between the mode volume V_m and the nonlinear coupling coefficients. In the hotspot region, the coupling can be expressed as $\beta_i \sim g\,\chi^{(2)}/\sqrt{V_\mathrm{m}}$, where g denotes the fraction of the electromagnetic energy localized within the singularity region. In the non-singular region, the coupling is $\beta_i' \sim (1-g)\,\chi^{(2)}/\sqrt{V_\mathrm{m}'}$. The total nonlinear coupling is then given by the sum $\beta_\mathrm{total} = \beta_i + \beta_i'$. Notably, although the calculated mode volume in the hotspot is very small, the overall SHG enhancement is limited by the coupling between the CBG and the bowtie nanocavity.

3.3 | Comparison of Bowtie-Integrated and Suspended CBG Structures for SHG

The lattice of LN belongs to the R3c space group, with threefold rotational symmetry along its optical axis. Based on this symmetry, the y- and z-component nonlinear polarization can be written as:

$$\begin{aligned} \mathbf{P}_y &= \varepsilon_0\left(-d_{22}\mathbf{E}_x^2 + d_{22}\mathbf{E}_y^2 + 2d_{31}\mathbf{E}_y\mathbf{E}_z\right), \\ \mathbf{P}_z &= \varepsilon_0\left(d_{31}\mathbf{E}_x^2 + d_{31}\mathbf{E}_y^2 + d_{33}\mathbf{E}_z^2\right), \end{aligned} \tag{1}$$

where $d_{22} = d_{21} = 2.1\ \mathrm{pmV^{-1}}$, $d_{31} = -4.3\ \mathrm{pmV^{-1}}$, and $d_{33} = -27\ \mathrm{pmV^{-1}}$. $\mathbf{E}$ is the electric field, and ε_0 is the vacuum permittivity. The phase-matching condition is significantly loosened at the nanoscale, as the wave interaction length is much shorter than the coherent buildup length. The second harmonic conversion efficiency reaches its maximum when the polarization angle of the incident light is aligned along the z-direction (optical axis). Therefore, we investigated the nonlinear enhancement factor along the crystal axis, which yields the strongest enhancement efficiency. In the experiment, the pump light, with a pulse width of 220 ps and a full width at half maximum (FWHM) spectral bandwidth of 1.9 nm, is filtered from a supercontinuum source using a tunable narrow bandpass optical filter. The FH spectrum is shown in Figure 4a. The FH wave at the resonant wavelength is tightly focused onto the sample using an objective lens with a numerical aperture (NA) of 0.65, see also Methods for details about the experimental setup. The maximum incident power on the sample is measured to be 0.21 mW, yielding a high normalized conversion efficiency of $0.85 \times 10^{-2}\ \mathrm{cm^2GW^{-1}}$ under a pump intensity of 1 $\mathrm{MWcm^{-2}}$, see also Tables S1 and S2.

The FH pump corresponding to the structural resonance under different periods and duty cycles is extracted to evaluate the enhancement of the SHG signal. The FH spectra are presented in the upper panels of Figure 4b,c, and the corresponding enhancement factors are shown in the lower panels. Blue denotes the bowtie-in-CBG structure, and red denotes the suspended CBG without the bowtie. A maximum enhancement factor of up to 3,720 is achieved for the bowtie-in-CBG structure compared to bare TFLN. In the design, the Bowtie structure is required to be minimized in size. For structures with small periods and low duty cycles, the relative size of the Bowtie is small. Consequently, the introduction of Bowtie-in CBG does not yield a noticeable enhancement under certain period and duty-cycle conditions. However, a pronounced enhancement effect is observed at large periods and high duty cycles. It is worth noting that the overall SHG reflection intensity of the 400-nm-thick TFLN is about ten times stronger than that of the 300-nm-thick sample at the same excitation wavelength of 1310-nm (see Figure S13). To demonstrate the compactness of the sample, the structure is designed with only 10 Bragg rings, resulting in an enhancement factor spanning three orders of magnitude. At extremely low incident pump power, visible SHG signals can be directly observed, as shown in Figure 4d; see also the Movie S1. The remarkably low incident pump power greatly extends the device lifetime, laying the foundation for stable and efficient quantum entanglement applications.

Figures 5a–c compare the SHG emission from three different structures, i.e., the bare TFLN, suspended CBG, and bowtie in suspended CBG. The enhancement of CGB and further enhancement of bowtie-in-CBG is evident. Nonetheless, the inherent diffraction limit precludes the direct spatial resolution of the enhancement localized at the apex. The enhancement within the hotspot gap of the bowtie is expected to be significantly stronger. This requires higher-resolution imaging technique, like scanning near-field optical microscopy (SNOM), to map the local field distribution. However, due to the experimental limitations, only a preliminary analysis of the near-field enhancement is conducted. The simulated variation of the electric and magnetic field with gap spacing is provided in Figure S10.

Furthermore, the SHG signal spectra of bowtie-integrated suspended CBG with different periods are detected, and the SHG signal is significantly enhanced compared to the background signal. As shown in Figure 5d, with the increase in period, the resonance peak shows a clear redshift. The SHG signal exhibits a clear quadratic relationship with the fundamental pump intensity (Figure 5e). In the log–log plot, the slope is 2.21, confirming the presence of second-order nonlinearity. Additionally, the relationship between the SHG signal and the polarization of the pump light is tested (Figure 5f). The second harmonic enhancement is strongest when the incident light is aligned along the crystal axis. Both tests indicate that the observed signal arises from the second-order nonlinear effect.

4 | Conclusion

In this work, a bowtie nanostructure integrated within a suspended circular Bragg cavity is experimentally demonstrated with giant SHG enhancement beyond the diffraction limit. The CBG

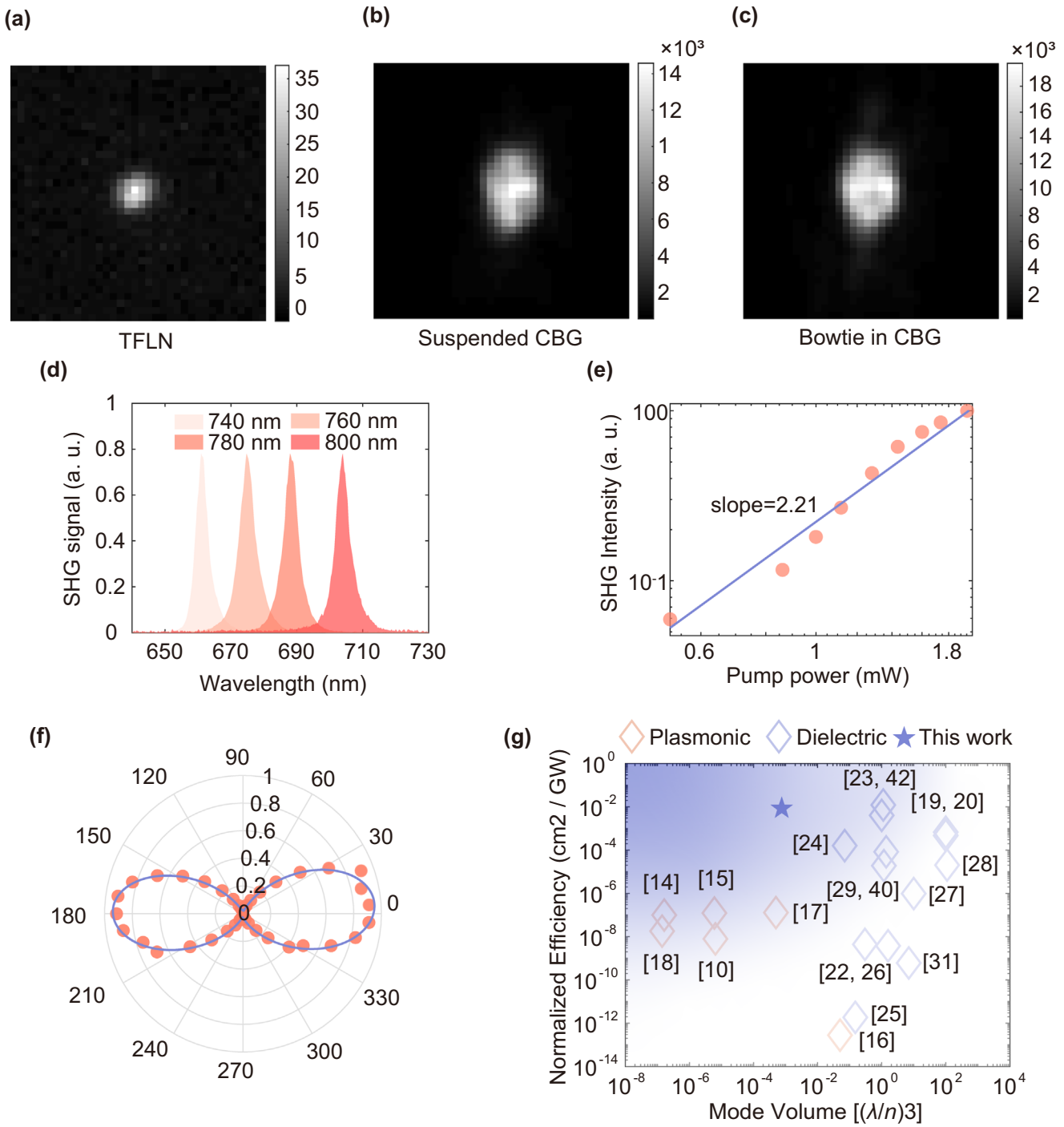

FIGURE 5 | Characterization of the SHG performance. (a–c) Microscopy images of SHG spots on (a) bare TFLN, (b) suspended CBG, and (c) bowtie structure in suspended CBG, respectively. (d) SHG spectra of bowtie in suspended CBG with the periods of 740, 760, 780, and 800 nm. (e) Log–log plot showing the quadratic relationship between the SH and FH powers in the bowtie structure within the suspended CBG, with pump wavelength $P = 760$ nm and duty cycle $D = 0.63$. (f) Polarization dependence of SHG power under the resonant FH pump. (g) Comparison of SHG conversion efficiency of different structures.

nanocavity achieves a high normalized conversion efficiency of 0.85×10^{-2} cm^{2}GW^{-1} under a pump intensity of 1 MWcm^{-2}, with a mode volume as small as 6.96×10^{-4} $(\lambda/n)^3$. An SHG enhancement factor of 3,720 is achieved compared to bare TFLN. Efficient SHG under ultralow pump intensities is demonstrated, significantly improving both the device performance and operational lifetime, while simultaneously reducing the mode volume.

In contrast to plasmonic resonances, the bowtie-integrated CBG structure is free from thermal losses and supports higher optical powers, significantly extending the upper limit of nonlinear conversion efficiency while maintaining an ultrasmall mode volume. Furthermore, compared to other all-dielectric nanostructures, our design exhibits a significantly reduced mode volume while maintaining a high SHG efficiency. The comparative results are

shown in Figure 5g and Table S3. Notably, this work represents the first experimental realization of a nonlinear optical response beyond the diffraction limit in an all-dielectric resonator.

In addition, we have demonstrated that a suspended circular Bragg cavity with only a few rings can achieve strong field localization, reducing the device footprint to below 10-μm. Compared to metalens arrays and BIC metasurfaces, this system offers higher nonlinear efficiency and greater compactness, providing a promising platform for compact, room-temperature multiphoton entanglement applications.

In summary, our work confirms the feasibility of achieving enhanced SHG in all-dielectric nanocavities to break the diffraction limit by integrating a bowtie nanoantenna into a suspended CBG nanocavity. The infinite singularity of the electric field at the apices of the dielectric bowtie nanoantenna enables extreme field localization, leading to a subdiffraction-limited mode volume with significant second-order nonlinearity enhancement in the bowtie-in-CBG nanocavity on the TFLN platform. The work opens new avenues for nonlinear photonics beyond the diffraction limit. Achieving ultralow mode volumes is crucial for practical applications in nonlinear nanophotonics. Strong field confinement not only enhances light–matter interaction and nonlinear conversion efficiency but also enables single-photon nonlinear processes. The ultralow mode volumes of these structures offer transformative potential. These effects are particularly important for on-chip quantum photonics, integrated nonlinear optical devices, and nanoscale frequency conversion. Such capabilities are essential for nano-lasers, nonlinear optics, photocatalysis, super-resolution techniques, quantum sources, and quantum computing, highlighting the transformative potential of structures with ultralow mode volumes.

5 | Methods

5.1 | Theoretical Calculations and Numerical Simulations

The suspended circular Bragg gratings were engineered with a tailored radial period to support resonant operation across the 1250–1500 nm wavelength range. Starting from the nonlinear Maxwell–s equations and assuming a time-harmonic electric field of the form $\mathbf{E}(\mathbf{r},t)=\mathbf{E}(\mathbf{r})e^{-i\omega t}$, the numerical simulations were performed using the finite-difference time-domain method.

In the absence of electrostatic interactions–that was, neglecting the free charge density ($\rho_f=0$) and the free current density ($\mathbf{J}_f=0$)–the nonlinear Maxwell's equations can be simplified under the high-frequency approximation (e.g., in the optical regime).

Based on the symmetry properties of TFLN, the nonlinear electric displacement field $\mathbf{D}(\omega)$ can be explicitly derived as:

$$\begin{pmatrix}\mathbf{D}_x(\omega)\\ \mathbf{D}_y(\omega)\\ \mathbf{D}_z(\omega)\end{pmatrix}=\varepsilon_0\begin{pmatrix}\varepsilon_{xx}(\omega)\mathbf{E}_x(\omega)+2d_{15}\mathbf{E}_y(\omega)\mathbf{E}_z(\omega)\\ \varepsilon_{yy}(\omega)\mathbf{E}_y(\omega)+2d_{15}\mathbf{E}_x(\omega)\mathbf{E}_z(\omega)\\ \varepsilon_{zz}(\omega)\mathbf{E}_z(\omega)+d_{31}\left(\mathbf{E}_x^2(\omega)+\mathbf{E}_y^2(\omega)\right)+d_{33}\mathbf{E}_z^2(\omega)\end{pmatrix} \tag{2}$$

This expression accounts for both the linear and second-order nonlinear polarization contributions permitted by the crystal symmetry of LN.

If only the anisotropy of the linear refractive index was considered, the solution of the electromagnetic field in cylindrical coordinates could be classified into two types, depending on whether the bowtie structure is present at the center.

5.1.1 | Regular Case Without Singularities

In typical cylindrical geometries where the domain includes the origin ($\rho=0$) and no geometric singularities are present, the solution to the radial equation must remain finite at $\rho=0$. Since the Bessel function of the second kind, $Y_{m_i}(k_i\rho)$, diverges at the origin, the physical requirement of regularity demands that its contribution be excluded. Thus, the general solution simplifies to:

$$R_i(\rho)=A_iJ_{m_i}(k_i\rho), \tag{3}$$

where $J_{m_i}(k_i\rho)$ is the Bessel function of the first kind, and A_i is a constant determined by boundary conditions.

5.1.2 | Case with Bowtie-Shaped Singularities

In contrast, when a bowtie-shaped singularity–such as a sharp metallic tip or a subwavelength dielectric gap–was present near or at $\rho=0$, the center was no longer a regular point in the domain. Such geometric features introduce a physical or mathematical singularity that invalidates the regularity condition at the origin.

In this scenario, the solution to the radial equation must retain both Bessel functions:

$$R_i(\rho)=A_iJ_{m_i}(k_i\rho)+B_iY_{m_i}(k_i\rho), \tag{4}$$

In this case, B_i is nonzero, leading to a divergent electric field at the singularity. The divergent nature of Y_{m_i} at the origin is therefore not unphysical, but may instead reflect genuine field enhancement resulting from the singular geometry. Such effects were particularly pronounced in dielectric nanogaps or nonlinear optical hotspots, where geometric singularities give rise to strong localized field amplification. Neglecting higher-order small terms of the electric field, the eigenmodes **E** and **H** are expressed as in Equation (S21).

5.2 | Fabrication of Suspended Circular Bragg Cavity

The suspended circular Bragg cavities were fabricated on a 400-nm thick x-cut TFLN (NANOLN), bonded on a 4.7-μm thick silica buffering layer and a 500-μm thick silicon substrate. First, A layer of 600-nm amorphous silicon is grown on TFLN by plasma enhanced chemical vapor deposition (PECVD). Next, a layer of polymethyl methacrylate (Zep520A) photoresist is spin-coated on the TFLN chip at a speed of 4000 rpm and baked at 180°C for 3 min. Then, the mask for CBGs and EBGs patterns was defined

using electron beam lithography (EBL), with a spot size of 5 nm and beam current of 2 nA. After EBL, the Zep520A photoresist was developed for 70 s in Pentyl acetate developer and fixed with IPA for 1 minute. The pattern of amorphous silicon was used as a hard mask during inductively coupled plasma reactive ion etching (ICP-RIE) process. Finally, CBGs were obtained after ICP-RIE and selective etching (Uetch-SyS VHF Etch System) of the silica buffering layer.

5.3 | Experimental Setup for Spectroscopy and SHG Measurement

The light source was a picosecond supercontinuum laser with a pulse duration of 220 ps (YSL photonics SC-pro, repetition rate: 20 MHz). The supercontinuum was first filtered by a long-pass filter (>1250 nm). The input light was then tightly focused on the sample by a NIR microscope objective (Mitutoyo 50×, NA = 0.65). Reflection light was collected by the same objective and reflected by a beam splitter (50:50, 600–1700 nm). A flip mirror was added after the beam splitter to guide the beam into two arms. The light was either coupled into a multimode fiber and recorded by a spectrometer or imaged using a camera (EMCCD, iXon Ultra 897). During the SHG characterization, the supercontinuum was filtered by a tunable narrow optical filter (YSL photonics AOTF-PRO2, FHWM 1.9 nm), and the beam was tightly focused onto the sample. The intensity of the reflected signal was measured using an EMCCD.

5.4 | Calculation of SHG Conversion Efficiency

The EMCCD pixel intensity was pre-calibrated using a light signal at the same wavelength (655 nm) range as the SHG signal. A photodiode power meter (Thorlabs, S130C, 400–1100 nm) measured the intensity of the known signal as 5 nW. The light spot was focused onto the EMCCD to integrate the signal, and the exposure time was recorded. The power was mapped with the sum count of $N_{\max}$. The exposure parameter was 0.001 ms. The CCD exposure time t_{ex} was linearly proportional to its count. Thus, the SHG signal with a sum count of N is calibrated as: $P_{SH} = \frac{N/t_{ex}}{N_{\max}/(0.001\ \text{ms})} \times 5\ \text{nW}$.

During the experiment, two short-pass filters (OD > 7) are used to filter the FH wave. The SHG conversion efficiency is defined as $\eta = P_{SH}/P_{FH}$, where P_{SH} and P_{FH} are the average powers of the SHG signal and FH, respectively. The power focused onto the sample is approximately 0.21 mW.

The peak intensity $\hat{P}_{FH}$ is calculated as: $\hat{P}_{FH} = P/(f\tau)$, where f is the pulse repetition rate and $\tau = 220$ ps is the pulse duration. The normalized SHG conversion efficiency η_{norm} is calculated as: $\eta_{\text{norm}} = \eta S/\hat{P}_{FH}$, where S is the focused beam area, with the spot diameter given by $\delta = 1.22\lambda/\text{N.A.} = 2.46\ \mu\text{m}$.

Author Contributions

Y.Z., Z.L., and X.C. conceived the idea and supervised the project. Z.L. and Z.H. developed the theory and performed the simulation. Z.L., G.W., H.L., and S.L. designed and fabricated the samples. Z.L., Z.H., and W.W. performed the experiments and data analysis. Z.L., Y.Z., and B.W. wrote the manuscript with the input from all authors.

Acknowledgements

This work was supported by the National Key Research and Development Program of China (2023YFB3906400, 2023YFA1407200); National Natural Science Foundation of China (12192252, 12504390); Science and Technology Commission of Shanghai Municipality (24JD1401700); Shanghai Municipal Science and Technology Major Project (2019SHZDZX01-ZX06); Yangyang Development Fund.

Conflicts of Interest

The authors declare no conflicts of interest.

Data Availability Statement

All data needed to evaluate the conclusions in the paper are present in the paper and/or the Supplementary Information.

References

1. Y. Wang, J. Yu, Y. F. Mao, et al., "Stable, High-Performance Sodium-Based Plasmonic Devices in the Near Infrared," *Nature* 581, no. 7809 (2020): 401–405.

2. Y. H. Ouyang, H. Y. Luan, Z. W. Zhao, W. Z. Mao, and R. M. Ma, "Singular Dielectric Nanolaser With Atomic-Scale Field Localization," *Nature* 632, no. 8024 (2024): 287–293.

3. W. Liu, Q. Zhu, C. N. Yang, et al., "Single-Molecule Sensing Inside Stereo- and Regio-Defined Hetero-Nanopores," *Nature Nanotechnology* 19, no. 11 (2024): 1693–1701.

4. E. Deist, J. A. Gerber, Y. H. Lu, J. Zeiher, and D. M. Stamper-Kurn, "Superresolution Microscopy of Optical Fields Using Tweezer-Trapped Single Atoms," *Physical Review Letters* 128, no. 8 (2022): 083201.

5. M. Kauranen and A. V. Zayats, "Nonlinear Plasmonics," *Nature Photonics* 6, no. 11 (2012): 737–748.

6. G. Li, S. Zhang, and T. Zentgraf, "Nonlinear Photonic Metasurfaces," *Nature Reviews Materials* 2, no. 5 (2017): 1–14.

7. T. Santiago-Cruz, S. D. Gennaro, O. Mitrofanov, et al., "Resonant Metasurfaces for Generating Complex Quantum States," *Science* 377, no. 6609 (2022): 991–995.

8. J. Zhang, J. Ma, M. Parry, et al., "Spatially Entangled Photon Pairs From Lithium Niobate Nonlocal Metasurfaces," *Science Advances* 8, no. 30 (2022): eabq4240.

9. Z. Wang, B. Li, N. Lu, et al., "Highly Efficient Ultraviolet Harmonic Generation Based on Coupled Guided Mode Resonances in Lithium Niobate Metasurfaces," *Laser & Photonics Reviews* 19, no. 22 (2025): e01010.

10. D. K. Gramotnev and S. I. Bozhevolnyi, "Plasmonics Beyond the Diffraction Limit," *Nature Photonics* 4, no. 2 (2010): 83–91.

11. M. Celebrano, X. Wu, M. Baselli, S. Großmann, et al., "Mode Matching in Multiresonant Plasmonic Nanoantennas for Enhanced Second Harmonic Generation," *Nature Nanotechnology* 10, no. 5 (2015): 412–417.

12. M. K. Kim, H. Sim, S. J. Yoon, et al., "Squeezing Photons Into a Point-Like Space," *Nano Letters* 15, no. 6 (2015): 4102–4107.

13. J. B. Khurgin, "Ultimate Limit of Field Confinement by Surface Plasmon Polaritons," *Faraday Discussions* 178 (2015): 109–122.

14. J. B. Khurgin, "How to Deal With the Loss in Plasmonics and Metamaterials," *Nature Nanotechnology* 10, no. 1 (2015): 2–6.

15. G. C. Li, D. Lei, M. Qiu, W. Jin, S. Lan, and A. V. Zayats, "Light-Induced Symmetry Breaking for Enhancing Second-Harmonic Generation From

an Ultrathin Plasmonic Nanocavity," *Nature Communications* 12, no. 1 (2021): 4326.

16. Z. Li, X. Ye, Z. Hu, et al., "Plasmonic Hotspot Arrays Boost Second Harmonic Generation in Thin-Film Lithium Niobate," *Optics Express* 32, no. 8 (2024): 13140–13155.

17. M. Galanty, O. Shavit, A. Weissman, et al., "Second Harmonic Generation Hotspot on a Centrosymmetric Smooth Silver Surface," *Light: Science & Applications* 7, no. 1 (2018): 49.

18. J. Li, G. Hu, L. Shi, et al., "Full-Color Enhanced Second Harmonic Generation Using Rainbow Trapping in Ultrathin Hyperbolic Metamaterials," *Nature Communications* 12, no. 1 (2021): 6425.

19. T. Zhang, Q. Guo, Z. Shi, S. Zhang, and H. Xu, "Coherent Second Harmonic Generation Enhanced by Coherent Plasmon–Exciton Coupling in Plasmonic Nanocavities," *ACS Photonics* 10, no. 5 (2023): 1529–1537.

20. L. Qu, Z. Gu, C. Li, et al., "Bright Second Harmonic Emission From Photonic Crystal Vertical Cavity," *Advanced Functional Materials* 33, no. 47 (2023): 2308484.

21. L. Bai, L. Qu, W. Wu, et al., "Wavelength-Tunable Second Harmonic Generation From Photonic Crystal Vertical Cavities," *Advanced Optical Materials* 13, no. 8 (2025): 2402686.

22. Z. Liu, B. Chen, X. Wang, et al., "Enhanced Vertical Second Harmonic Generation From Layered GaSe Coupled to Photonic Crystal Circular Bragg Resonators," *Nanophotonics* 13, no. 21 (2024): 4029–4035.

23. X. Wang, Z. Liu, B. Chen, G. Qiu, D. Wei, and J. Liu, "Experimental Demonstration of High-Efficiency Harmonic Generation in Photonic Moiré Superlattice Microcavities," *Nano Letters* 24, no. 36 (2024): 11327–11333.

24. X. Ye, G. Wang, X. Duan, et al., "Near-Field Vortex Dynamics of Supercell Bloch Modes," *Physical Review Letters* 134, no. 24 (2025): 243801.

25. A. P. Anthur, H. Zhang, R. Paniagua-Dominguez, et al., "Continuous-Wave Second Harmonic Generation Enabled by Quasi-Bound States in the Continuum on Gallium Phosphide Metasurfaces," *Nano Letters* 20, no. 12 (2020): 8745–8751.

26. K. Koshelev, S. Kruk, E. Melik-Gaykazyan, et al., "Subwavelength Dielectric Resonators for Nonlinear Nanophotonics," *Science* 367, no. 6475 (2020): 288–292.

27. L. Wang, Z. Yang, S. Li, et al., "Reversible Thermal Tuning of High-*Q* Nonlocal Lithium Niobate Metasurfaces," *Laser & Photonics Reviews* 20, no. 5 (2026): e02038.

28. M. Nauman, J. Yan, D. de Ceglia, et al., "Tunable Unidirectional Nonlinear Emission From Transition-Metal Dichalcogenide Metasurfaces," *Nature Communications* 12, no. 1 (2021): 5597.

29. A. A. Popkova, I. M. Antropov, G. I. Tselikov, et al., "Nonlinear Exciton–Mie Coupling in Transition-Metal Dichalcogenide Nanoresonators," *Laser & Photonics Reviews* 16, no. 6 (2022): 2100604.

30. J. Ma, F. Xie, W. Chen, et al., "Nonlinear Lithium Niobate Metasurfaces for Second Harmonic Generation," *Laser & Photonics Reviews* 15, no. 5 (2021): 2000521.

31. S. Yuan, Y. Wu, Z. Dang, et al., "Strongly Enhanced Second Harmonic Generation in a Thin-Film Lithium Niobate Heterostructure Cavity," *Physical Review Letters* 127, no. 15 (2021): 153901.

32. M. Timofeeva, L. Lang, F. Timpu, et al., "Anapoles in Free-Standing III–V Nanodisks Enhancing Second-Harmonic Generation," *Nano Letters* 18, no. 6 (2018): 3695–3702.

33. Y. Li, Z. Huang, Z. Sui, et al., "Optical Anapole Mode in Nanostructured Lithium Niobate for Enhancing Second Harmonic Generation," *Nanophotonics* 9, no. 11 (2020): 3575–3585.

34. G. Zograf, A. Y. Polyakov, M. Bancerek, T. J. Antosiewicz, B. Küçüköz, and T. O. Shegai, "Combining Ultrahigh Index With Exceptional Nonlinearity in Resonant Transition-Metal Dichalcogenide Nanodisks," *Nature Photonics* 18, no. 7 (2024): 751–757.

35. R. Biswas, A. Prosad, L. K. AS, et al., "Leveraging Strong Electric Field Gradients at Anapole Resonances for Enhanced Second Harmonic Generation From Molybdenum Disulfide Disks," *Advanced Materials* 37, no. 14 (2025): 2418257.

36. H. Shim, F. Monticone, and O. D. Miller, "Fundamental Limits to the Refractive Index of Transparent Optical Materials," *Advanced Materials* 33, no. 43 (2021): 2103946.

37. J. B. Khurgin, "Expanding the Photonic Palette: Exploring High-Index Materials," *ACS Photonics* 9, no. 3 (2022): 743–751.

38. H. Choi, M. Heuck, and D. Englund, "Self-Similar Nanocavity Design With Ultrasmall Mode Volume for Single-Photon Nonlinearities," *Physical Review Letters* 118, no. 22 (2017): 223605.

39. S. Hu, M. Khater, R. Salas-Montiel, et al., "Experimental Realization of Deep-Subwavelength Confinement in Dielectric Optical Resonators," *Science Advances* 4, no. 8 (2018): eaat2355.

40. M. Albrechtsen, B. Vosoughi Lahijani, R. E. Christiansen, et al., "Nanometer-Scale Photon Confinement in Topology-Optimized Dielectric Cavities," *Nature Communications* 13, no. 1 (2022): 6281.

41. A. N. Babar, T. A. S. Weis, K. Tsoukalas, et al., "Self-Assembled Photonic Cavities With Atomic-Scale Confinement," *Nature* 624, no. 7990 (2023): 57–63.

42. S. Gafsi and J. D. Ryckman, "All-Dielectric Metawaveguide Ring Resonators With Deeply Sub-Diffractive Mode Volumes," *Laser & Photonics Reviews* 19, no. 11 (2025): 2401579.

43. C. Wang, M. Zhang, X. Chen, et al., "Integrated Lithium Niobate Electro-Optic Modulators Operating at CMOS-Compatible Voltages," *Nature* 562, no. 7725 (2018): 101–104.

44. L. Qu, L. Bai, C. Jin, et al., "Giant Second Harmonic Generation From Membrane Metasurfaces," *Nano Letters* 22, no. 23 (2022): 9652–9657.

45. A. Boes, L. Chang, C. Langrock, et al., "Lithium Niobate Photonics: Unlocking the Electromagnetic Spectrum," *Science* 379, no. 6627 (2023): eabj4396.

46. Z. Li, Z. Hu, X. Ye, et al., "Enhanced Second-Harmonic Generation in Thin-Film Lithium Niobate Circular Bragg Nanocavity," *Nano Letters* 24, no. 37 (2024): 11676–11682.

47. H. Wang, Y. M. He, T. H. Chung, et al., "Towards Optimal Single-Photon Sources From Polarized Microcavities," *Nature Photonics* 13, no. 11 (2019): 770–775.

48. O. Iff, Q. Buchinger, M. Moczała-Dusanowska, et al., "Purcell-Enhanced Single-Photon Source Based on a Deterministically Placed WSe_2 Monolayer Quantum Dot in a Circular Bragg Grating Cavity," *Nano Letters* 21, no. 11 (2021): 4715–4720.

Supporting Information

Additional supporting information can be found online in the Supporting Information section.

Supporting File 1: lpor71263-sup-0001-SuppMat.pdf.

Supporting File 2: lpor71263-sup-0002-Movie.mp4.